



HAL
open science

Surface Flow from Visual Cues

Benjamin Petit, Antoine Letouzey, Edmond Boyer

► **To cite this version:**

Benjamin Petit, Antoine Letouzey, Edmond Boyer. Surface Flow from Visual Cues. [Research Report] RR-7619, 2011, pp.18. inria-00593206v1

HAL Id: inria-00593206

<https://inria.hal.science/inria-00593206v1>

Submitted on 16 May 2011 (v1), last revised 17 May 2011 (v2)

HAL is a multi-disciplinary open access archive for the deposit and dissemination of scientific research documents, whether they are published or not. The documents may come from teaching and research institutions in France or abroad, or from public or private research centers.

L'archive ouverte pluridisciplinaire **HAL**, est destinée au dépôt et à la diffusion de documents scientifiques de niveau recherche, publiés ou non, émanant des établissements d'enseignement et de recherche français ou étrangers, des laboratoires publics ou privés.



INSTITUT NATIONAL DE RECHERCHE EN INFORMATIQUE ET EN AUTOMATIQUE

Surface Flow from Visual Cues

Benjamin Petit — Antoine Letouzey — Edmond Boyer

N° 7619

May 2011

Domaine 4



*R*apport
de recherche

Surface Flow from Visual Cues

Benjamin Petit, Antoine Letouzey, Edmond Boyer

Domaine : Perception, cognition, interaction
Équipe-Projet Morpheo

Rapport de recherche n° 7619 — May 2011 — 18 pages

Abstract: In this paper we study the estimation of dense, instantaneous 3D motion fields over non-rigidly moving surface observed by multi-camera systems. The motivation arises from multi-camera applications that require motion information for arbitrary subjects, in order to perform tasks such as surface tracking or segmentation. To this aim, we present a novel framework that allows to efficiently compute dense 3D displacement fields using low level visual cues and geometric constraints. The main contribution is a unified framework that combines flow constraints for small displacements with temporal feature constraints for large displacements and fuses them over the surface using local rigidity constraints. The resulting linear optimization problem allows for variational solutions and fast implementations. Experiments conducted on synthetic and real data demonstrate the respective interests of flow and feature constraints as well as their efficiency to provide robust surface motion cues when combined.

Key-words: Surface, flow, 3D motion

Flot de surface à partir d'indices visuels

Résumé : Dans ce papier nous nous intéressons à l'estimation des champs de déplacement denses d'une surface non rigide, en mouvement, capturée par un système multi-caméra. La motivation vient des applications multi-caméra qui nécessitent une information de mouvement pour accomplir des tâches telles que le suivi de surface ou la segmentation. Dans cette optique, nous présentons une approche nouvelle, qui permet de calculer efficacement un champ de déplacement 3D, en utilisant des informations visuelles de bas niveau et des contraintes géométriques. La contribution principale est la proposition d'un cadre unifié qui combine des contraintes de flot pour de petits déplacements et des correspondances temporelles éparées pour les déplacements importants. Ces deux types d'informations sont fusionnés sur la surface en utilisant une contrainte de rigidité locale. Le problème se formule comme une optimisation linéaire permettant une implémentation rapide grâce à une approche variationnelle. Les expérimentations menées sur des données synthétiques et réelles démontrent les intérêts respectifs du flot et des informations éparées, ainsi que leur efficacité conjointe pour calculer les déplacements d'une surface de manière robuste.

Mots-clés : Surface, flot, déplacements 3D

Contents

1	Introduction	3
2	Related Work	4
3	Preliminaries and Definitions	5
4	Visual Constraints	6
4.1	Dense 2D Normal Flow	7
4.2	Sparse 2D Features	7
4.3	Sparse 3D Features	8
5	Regularization	9
5.1	Deformation Model	9
5.2	Energy Functional Minimization	10
5.3	Selection of Weights and 2-Pass Refinement	10
6	Evaluation	11
6.1	Quantitative Evaluation on Synthetic Data	12
6.2	Comparison	13
6.3	Experiments on Real Data	14
7	Conclusion	14

1 Introduction

Recovering dense motion information is a fundamental intermediate step in the image processing chain upon which higher level applications can be built, such as tracking or segmentation. For that purpose, pixel observations in the image provide useful motion cues through temporal variations of the intensity function. In the monocular case these variations allow to recover a dense 2D motion field in the image: the *optical flow*. The estimation of the optical flow has been a subject of interest in the vision community for decades and numerous methods Barron et al. (1994); Horn and Schunck (1981); Lucas and Kanade (1981) have been proposed. In the multiocular case, the integration over different viewpoints allow to consider 3D motions of points on the observed surfaces and to estimate dense 3D vector fields: the *scene flow* Neumann and Aloimonos (2002); Vedula et al. (2005). However, in both 2D and 3D cases, the motion information cannot be determined independently at a point from intensity variations only and additional constraints between points must be introduced, smoothness for example. Moreover, as a result of finite difference approximations of derivatives, flow estimations are known to be limited to small motions. While several approaches have been proposed in 2D to cope with these limitations Xu et al. (2010), less efforts have been devoted to the 3D case.

In this paper we study how to incorporate, in an efficient way, various constraints when estimating dense motion information over 3D surfaces from temporal variations of the intensity function in several images. Our primary motivation is to provide robust motion cues that can be directly used by an application, e.g. interactive applications, or that can be fed into more advanced tasks such as surface tracking or segmentation, e.g. into rigid parts. The approach is however not limited to a specific scenario and applies



Figure 1: Example of dense scene flow (in blue) from sparse 2D and 3D features and dense normal flow constraints (as for the rest of the paper, figures are best viewed in color).

to any application that can benefit from low level motion information. Most existing approaches that estimate scene flow assume small motions between time instants for which finite difference approximations of temporal derivatives are valid. However this assumption is often violated with actual acquisition systems and real moving objects. In addition, flow constraints are usually plugged into specific resolution schemes that are not necessarily grounded on physical principles nor easily allow for constraints of different types to be taken into account.

We propose a unified framework that links visual constraints from consecutive images with surface deformation constraints in a consistent way. In order to handle large motions, it allows for local temporal matching constraints, as obtained with image features. Such features act as anchor points in surface regions with larger displacements and where pixel intensity variations are not informative. All visual constraints are *diffused* over the surface through a Laplacian scheme that regularizes the estimated motion vectors between neighboring surface points. A key feature of the proposed framework is that it leads to linear optimizations, enabling therefore fast implementations.

The remainder of this paper is as follows. Section §4 presents the visual constraints obtained from consecutive images. Section §5 explains how to integrate these constraints over the surface. Experimental results on both synthetic and real data are then presented in section §6 before discussing the approach in section §7.

2 Related Work

In a seminal work on scene flow, Vedula *et al.* Vedula et al. (2005) explicated the normal flow constraint that links the intensity function derivatives in images to the scene flow of 3D points. As mentioned before, such constraints do not allow to estimate the scene flow independently at a surface point and additional constraints must be introduced. Instead of using the normal flow constraint, an algorithm is proposed that linearly estimates the scene flow given the surface geometry and 2D optical flows. Optical flow

better constrains the scene flow than the normal flow, however their estimation is based on smoothness assumptions that seldom hold in the image planes whereas they often do on surfaces.

In Neumann and Aloimonos (2002), Neumann and Aloimonos introduced an elegant subdivision surface model that allows to integrate normal flow constraints over the surface with regularization constraints. Nevertheless, this global solution still assumes small motions and can hardly deal with challenging datasets as used in this paper.

Another strategy is followed by Pons *et al.* Pons *et al.* (2005) who presented a variational framework that optimizes a photo-consistency criterion instead of the normal flow constraints. The interest is that both spatial and temporal consistency can be enforced but at the price of a computationally expensive optimization. In contrast, our focus is not on shape optimization but more on providing low level motion information in an efficient way. Several works Isard and MacCormick (2006); Wedel *et al.* (2008); Zhang and Kambhampettu (2001) consider the case where the scene structure is described by stereo disparities and propose combined estimation of spatial disparity and temporal 3D motion. We consider a different situation where the shape surface is given, e.g. a mesh obtained using a multi-view approach, thus allowing for a regularization of the motion field over a domain where smoothness assumptions hold.

It is worth also mentioning recent approaches on temporal surface tracking Cagniard *et al.* (2010); Naveed *et al.* (2008); Starck and Hilton (2007b); Varanasi *et al.* (2008) that can also provide velocity fields as a by-product of the matching between consecutive frames. Our purpose is anyway different since our method does not make any assumption on the observed shape and only weak assumptions on the deformation model in the form of local smoothness assumptions. It provides information at a lower level, instant motion, that can in turn be used as input data by a surface tracking or matching approach.

Our contributions with respect to the aforementioned approaches are twofold: (i) Following works on robust optical flow estimation Liu *et al.* (2008); Xu *et al.* (2010), we take advantage of robust initial displacement values as provided by image features tracked over consecutive time instants. Such features allow for large surface motions while normal flow constraints better model small motions. (ii) A linear framework that combines visual constraints with surface deformation constraints and allows for iterative resolutions (variational approach) as well as coarse to fine refinement.

3 Preliminaries and Definitions

Our method deals with the output of any multi-camera system capable of producing a stream of non-rigidly moving surfaces, each independently reconstructed from a set of N calibrated views, using a 3D reconstruction technique such as Franco and Boyer (2008) or Furukawa and Ponce (2006).

The surface at time t is denoted $\mathcal{S}^t \subset \mathbb{R}^3$ and associated with the set of images $\mathcal{I}^t = \{\mathbf{I}_c^t \mid c \in [1..N]\}$. A 3D point \mathbf{P} on the surface is described by the 3D vector $(x, y, z)^T \in \mathbb{R}^3$. Its projection in the image \mathbf{I}_c^t is the 2D image point \mathbf{p}_c with coordinates $(u_c, v_c)^T \in \mathbb{R}^2$ computed using the 3x4 projection matrix $\mathbf{\Pi}_c : \mathbb{R}^3 \mapsto \mathbb{R}^2$ of camera c (see figure 2). The 2D image region corresponding to the visibility of \mathcal{S}^t in \mathbf{I}_c^t is denoted by $\Omega_c^t = \mathbf{\Pi}_c \mathcal{S}^t$.

Our method is looking for the 3D motion field of the surface between time t and $t + 1$ described by $V^t : \mathcal{S}^t \mapsto \mathbb{R}^3$ with $V^t(\mathbf{P}) = \frac{d\mathbf{P}}{dt} \forall \mathbf{P} \in \mathcal{S}^t$. This motion field is

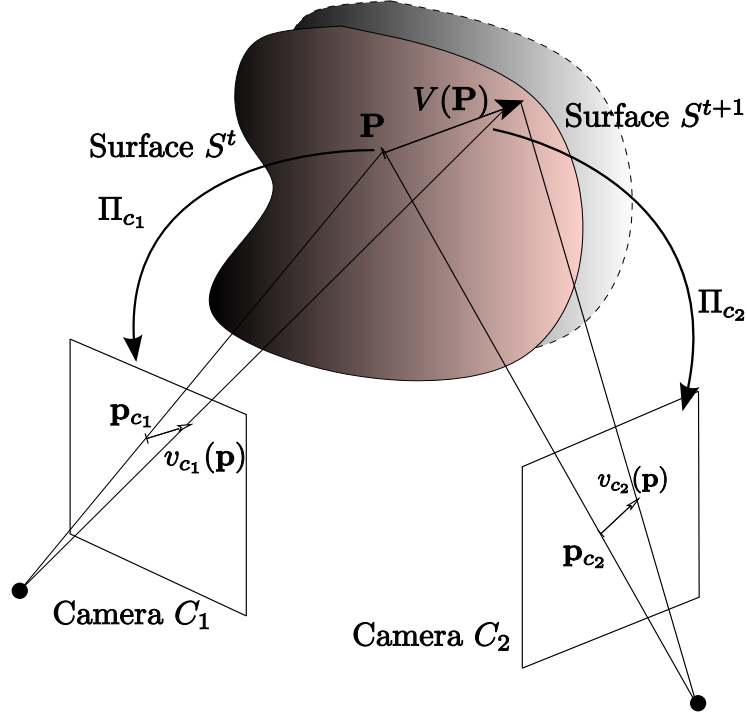


Figure 2: Projection from scene flow $V(P)$ into optical flows v_c^t in different images of a multi-camera system.

constrained by: (i) the input data, i.e. the set of calibrated images \mathcal{I}^t and \mathcal{I}^{t+1} and the surface S^{t+1} and (ii) a deformation model.

The projection of the 3D motion field on \mathbf{I}_c^t is denoted by v_c^t . The relation between a small displacement on the surface S^t and its image taken by the camera c is described by the 2x3 jacobian matrix $J_{\Pi_c}(\mathbf{p}_c) = \frac{\partial \mathbf{p}_c}{\partial \mathbf{P}}$ such that $v_c^t = J_{\Pi_c}(\mathbf{p}_c)V^t$.

4 Visual Constraints

Our method can use three types of visual constraints to estimate 3D displacements:

1. dense image flow constraints,
2. sparse 2D features correspondences, and
3. sparse 3D features correspondences.

Each of these constraints will lead to a term in the error functional (see section §5.2), describing how the computed 3D motion field relates to the observations. Notice that we do not include spatial or temporal photo-consistency constraints as they yield non-linear terms in the error and better adapt to shape optimization problems than to direct low level motion cue estimation.

4.1 Dense 2D Normal Flow

Dense information on V^t can be classically obtained using the 2D optical flow information available in the images. Indeed, assuming brightness constancy between \mathbf{p}_c^{t+1} and \mathbf{p}_c^t , projection of the same surface point on two consecutive frames, one can write the *Normal Flow Equation* Barron et al. (1994) as:

$$\begin{aligned} \nabla I_c^t \cdot v_c^t + \frac{dI_c^t}{dt} &= 0, \\ \text{or } \nabla I_c^t \cdot [J_{\Pi_c} V^t] + \frac{dI_c^t}{dt} &= 0, \end{aligned}$$

as expressed from 3D surface velocities Vedula et al. (2005); ∇I_c^t is the spatial gradient of the image intensity and $\frac{dI_c^t}{dt}$ is the temporal gradient of image intensity. We can then define an error term measuring the discrepancy between the computed 2D motion field v_c^t and the normal flow constraints:

$$\mathbf{E}_{flow} = \sum_{c=1}^N \int_{\Omega_c^t} \left\| \nabla I_c^t \cdot [J_{\Pi_c} V^t] + \frac{dI_c^t}{dt} \right\|^2 d\mathbf{p}_c. \quad (1)$$

This term is the most common among scene flow methods and well suited for small image displacements, but has important limitations: it only constrains the image displacements in the direction of the image gradient ∇I_c^t , or the normal component of the optical flow. This is the *aperture problem* in 2D that extends to 3D as will be discussed in 5. Also, linearization based on the image gradient is typically invalid for large displacements.

4.2 Sparse 2D Features

In some situations, e.g. slow motion or high frame rates, motion field recovery can rely on dense normal flow constraints alone. However, in a more general context, additional constraints must be considered. To this purpose, we propose the use of sparse 2D correspondences between the set of images \mathcal{I}^t and \mathcal{I}^{t+1} as 2D anchor points to guide the flow estimation. Such features are easily obtained using one of various popular techniques, e.g. SIFT Lowe (2004). Importantly, we opt to match features among subsequent frames of the same camera and not between views: First, this eliminates any need for inter-camera exposure and color calibration. More importantly, the match and outlier rates between such images are substantially more favorable than for inter-camera matching. This is especially true for the challenging data targeted: general subjects with low-to-average texture, object-centered setups exhibiting wide baselines by nature. Any remaining outliers can thus be easily eliminated using a conservative matching threshold, as validated in our experiments.

We compute SIFT descriptors for \mathcal{I}^t and \mathcal{I}^{t+1} , then match features between \mathbf{I}_c^t and \mathbf{I}_c^{t+1} , with $c \in [1..N]$. This yields a set of sparse 2D displacements $v_{c,s}^t$ for some 2D points $\mathbf{p}_{c,s} \in \Omega_c^t$, those points form a subset of Ω_c^t called $\Omega_{c,s}^t$ (see figure 3). The following error term measures the discrepancy between the computed 2D motion field

v_c^t and the sparse 2D displacements $v_{c,s}^t$:

$$\mathbf{E}_{2D} = \sum_{c=1}^N \sum_{\Omega_{c,s}^t} \|v_c^t - v_{c,s}^t\|^2, \text{ or}$$

$$\mathbf{E}_{2D} = \sum_{c=1}^N \sum_{\Omega_{c,s}^t} \|J_{\Pi_c} V^t - v_{c,s}^t\|^2, \quad (2)$$

where (2) is the linearization we use. Unlike the normal flow equation, this approximation is still valid for moderate displacements as it doesn't involve image gradients.

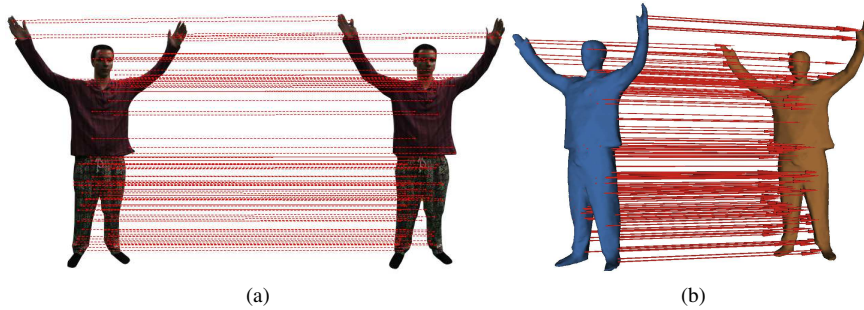


Figure 3: Example of sparse 2D features obtained from image matching (a), and 3D feature correspondences between two surfaces (b).

4.3 Sparse 3D Features

3D features can also easily be included in our framework to guide flow estimation in the presence of large displacements. They provide sparse displacement information for a set of salient 3D points lying on S^t , obtained by detecting features on S^t and S^{t+1} and matching them across time based on a geometric or photometric surface descriptor. These correspondences can be obtained using various recent methods, such as Starck and Hilton (2007a), or the MeshDOG 3D features detector and the MeshHOG descriptor Zaharescu et al. (2009), and can provide complementary information to the 2D terms previously described in the form of robustness to occlusions. On the other hand, they are sensitive to different issues, such as topology changes of the observed surface, which sometimes occur in the sequence.

We have found that an interesting trade-off to obtain 3D features is to back-project matching 2D feature correspondences between \mathcal{I}^t and \mathcal{I}^{t+1} onto their respective surfaces S^t and S^{t+1} . This yields a 3D point pair whose match was based on intra-view 2D SIFT. This is not entirely equivalent to the sparse 2D feature term previously proposed, as it assumes availability of S^{t+1} , when the latter could be used without, if required by the application. Also this type of match could be influenced by the error in surface estimation, dependent on the reconstruction method used. The advantage in having 3D constraints is that the term is valid for arbitrarily large displacements as it doesn't need linearization. We have found this scheme to work well in practice and use it in stages of the final algorithm described in section 5.3.

Regardless of how they are obtained, let V_m^t be the displacements of the detected feature points $\mathbf{P}_m \in \mathcal{S}^t$ (see figure 3). These points form a discrete subset of \mathcal{S}^t called \mathcal{S}_m^t . Being measured directly as a 3D distance, the error between the computed 3D motion field V^t and the target 3D displacements V_m^t can be written without linearization:

$$\mathbf{E}_{3D} = \sum_{\mathcal{S}_m^t} \|V^t - V_m^t\|^2 . \quad (3)$$

5 Regularization

The sparse set of 2D and 3D correspondences only constrains the displacement of the surface for specific 3D points and for their re-projection on the images. To find a dense motion field over the surface we need to propagate those constraints through a regularization term.

Furthermore, as mentioned earlier, dense 2D normal flow constraints do not provide enough information to estimate 3D displacements. In fact it can be shown that the normal flow equations at different image projections of a 3D point \mathbf{P} are linearly dependent, and can only solve 2 of the 3 dofs. Vedula *et al.* Vedula et al. (2005) mentioned two regularization strategies to cope with this limitation. The regularization can be performed in the image planes to estimate optical flows which provide then full constraints on the scene flow, or the regularization can be performed on the 3D surface.

Since we are given the 3D surface and that sparse constraints from 2D or 3D features need to be integrated, a natural choice in our context is to regularize in 3D. In addition regularization in the image space suffers from artifacts and incoherences resulting from depth discontinuities and occlusions that contradict the smoothness assumption whereas such assumption holds on the 3D surface.

5.1 Deformation Model

Smoothness assumptions on 3D displacements fields over a surface constrain the surface deformations locally. They thus define a deformation model of the surface, e.g. local rigidity. In 2D, numerous regularization schemes have been proposed for the optical flow estimation that fall into 2 main categories: local and global regularizations. They can be extended to 3D. For example, the 2D Lucas and Kanade method, which uses a local spatial neighborhood, was applied in 3D by Devernay *et al.* Devernay et al. (2006). However, the associated deformation model of the surface has no real meaning since deformation constraints only propagate locally, yielding inconsistencies between neighborhoods. On the other hand, the global strategy introduced by Horn and Schunck Horn and Schunck (1981) is well suited to our context. Though less robust to noise than local methods such as Lucas-Kanade, it allows sparse constraint propagation over the whole surface. In addition the associated surface deformation model has proved to be efficient in the computer graphics domain Sorkine and Alexa (2007).

The extension of Horn and Schunck deformation model to 3D points is described by the following error function which enforces a local rigidity of the motion field:

$$\mathbf{E}_d = \int_S \|\nabla V\|^2 d\mathbf{P} . \quad (4)$$

5.2 Energy Functional Minimization

We find the best displacement that satisfies all the aforementioned constraints by minimizing the following error functional:

$$\arg \min_V [\lambda_{3D}^2 \mathbf{E}_{3D} + \lambda_{2D}^2 \mathbf{E}_{2D} + \lambda_{flow}^2 \mathbf{E}_{flow} + \lambda_d^2 \mathbf{E}_d],$$

where the different λ coefficients are parameters that can be set to give more weight to a particular constraint.

This functional can be minimized by solving its associated Euler-Lagrange equation:

$$\sum_{c=1}^N \left[\lambda_{flow}^2 \left[\nabla I_c^t \cdot [J_{\Pi_c} V^t] + \frac{dI_c^t}{dt} \right] + \lambda_{2D}^2 \delta_{\Omega_{c,s}^t} J_{\Pi_c} [V^t - V_{c,s}^t] \right] + \lambda_{3D}^2 \delta_{\mathcal{S}_m^t} [V^t - V_m^t] + \lambda_d^2 \nabla^2 V^t = 0, \quad (5)$$

where δ is the Kronecker symbol, denoting that this constraint is only defined for 3D points in \mathcal{S}_m^t or $\Omega_{c,s}^t$.

The discretized Euler-Lagrange equation for each 3D points \mathbf{P} of the surface has the form:

$$\mathbf{A}_P V_P + \mathbf{b}_P - \Delta V_P = 0, \quad (6)$$

where Δ is the normalized Laplace-Beltrami operator over the surface.

The combination of equation (6) for all 3D points $\mathbf{P} \in \mathcal{S}^t$ creates a simple linear system of the form:

$$\begin{bmatrix} \mathbf{L} \\ \mathbf{A} \end{bmatrix} V^t + \begin{bmatrix} \mathbf{0} \\ \mathbf{b} \end{bmatrix} = 0, \quad (7)$$

where \mathbf{L} is the Laplacian matrix as defined in Sorkine and Alexa (2007). This is a sparse linear system which can be solved using a sparse solver such as *Taucs*.

Note that, interestingly, this formulation revisits the Laplacian mesh editing in an *as-rigid-as-possible* way of the computer graphics community Sorkine and Alexa (2007). While the deformation model is similar, the difference lies in the constraint used: anchor points in Sorkine and Alexa (2007) and visual constraints in our approach. In both cases, it is known that this deformation model does not handle explicitly rotations of the surface. Although this is an issue when deforming the surface under a small number of constraints, as usual in graphic applications, the density of the normal flow constraints in our case help recovering rotations without the need for nonlinear optimizations.

Equation (5) can also be solved iteratively using the Jacobi method applied to this large sparse system. In this case one could solve the linear system for each points independently and repeat the process iteratively using the updated solution of the neighborhood points. This variational approach allows as well for coarse to fine refinements.

5.3 Selection of Weights and 2-Pass Refinement

In equation (5), the parameters λ_{2D} , λ_{3D} , λ_{flow} and λ_d indicate the strengths of 2D and 3D features, 2D normal flow constraints and the Laplacian respectively. High values of the parameters imply that the influence of each of the respective components is larger.

In our context, similarly to Xu et al. (2010) in 2D, we trust our 2D and 3D features to be robust even under wide displacements, while we know that the 2D flow constraints are not reliable when the reprojected displacement is greater than a few

pixels on the images. Consequently, we propose a method that performs two consecutive minimizations of the energy functional using two sets of weights. The steps of the corresponding algorithm are as follows:

1. We start by computing the sparse 2D and 3D feature correspondences between \mathcal{S}^t and \mathcal{S}^{t+1} and between \mathcal{I}^t and \mathcal{I}^{t+1} . We also compute the Laplacian matrix \mathbf{L} of our discretized surface.
2. We solve equation (7), with $\lambda_{flow} = 0$ and high values of λ_{3D} and λ_{2D} with respect to λ_d . We obtain a first approximation of V^t denoted V'^t which recover wide displacements on the surface.
3. We create a deformed surface $\mathcal{S}'^t = \mathcal{S}^t + V'^t$ that we re-project in all cameras using the initial texture information coming from the projection of \mathcal{I}^t on \mathcal{S}^t . We obtain a new set of images \mathcal{I}'^t .
4. We compute the visibility of the surface \mathcal{S}'^t on each camera and the dense normal flow constraints between \mathcal{I}'^t and \mathcal{I}^{t+1} for each visible points. We thus have several constraints by sampled points of the surface.
5. As in step 2, we solve equation (7) using the flow computed in step 4 and the 2D and 3D features previously computed in step 1 as anchor points. For this step we use high values for λ_{3D} and λ_{2D} and lower values for λ_{flow} and λ_d . We obtain the displacement between \mathcal{S}'^t and \mathcal{S}^{t+1} denoted V''^t and thus a refined version of $V^t = V'^t + V''^t$. This second step allows us to recover smaller displacements, which is handled well by the flow constraint.

We see from our results that, in practice our approach can handle both large and small displacements. This is because we use sparse features to attain large displacements and the normal flow to recover the details.

6 Evaluation

For our evaluation we used both synthetic and real data:

1. Synthetic data were obtained deforming a model over time to create sequences. We rasterized this sequences into virtual cameras of resolution 1 MPixels, distributed on a sphere around the models. We used two different models and camera setups to create different sequences. (i) A triangular mesh with 7k vertices representing an articulated human model, deformed to generate a sequence of 200 frames viewed by ten cameras. (ii) A rigidly moving sphere model of 640 vertices viewed by 34 cameras, used for quantitative evaluation and comparison.
2. Real data are taken from publicly available datasets (or soon to be). We present experiments on the *flashkick* sequence from the *SurfCap* project Starck and Hilton (2007b) of University of Surrey. This sequence uses height 2 MPixels cameras, and produces smooth meshes of $\sim 140k$ vertices. The other sequences were taken from 32 2 MPixels cameras and provide visual-hull based meshes of $\sim 10k$ vertices.

See the accompanying video in supplemental material for more results.

6.1 Quantitative Evaluation on Synthetic Data

Using the algorithm described in section §5.3 we computed the motion fields on the synthetic dance sequence. Figure 4-a) shows the motion field on one frame of the sequence. Red vectors denote the initial sparse 3D and reprojected 2D constraints while blue vectors denote the sampled 3D motion field.

Figure 4-b) shows the motion field accumulated over few frames from a top view. This result can be somehow compared to the one from Varanasi *et al.* Varanasi et al. (2008), indeed their method is able to provide velocity field, albeit as a by-product of the matching between two consecutive meshes.

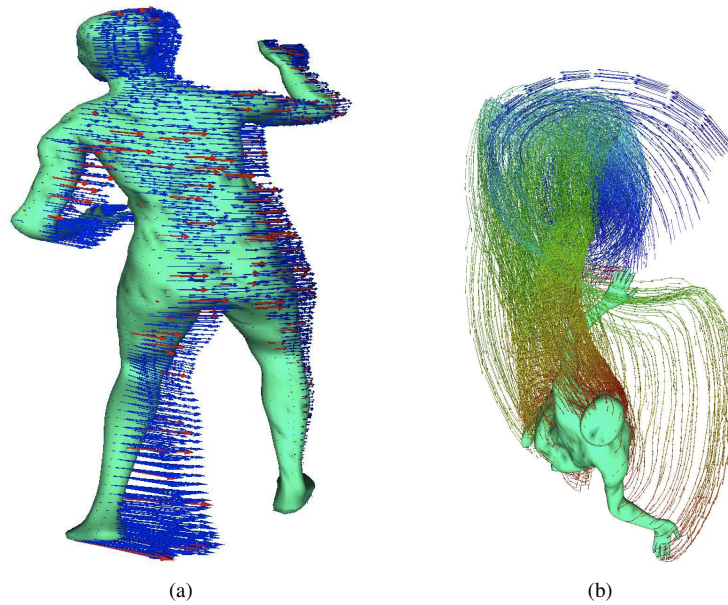


Figure 4: (a) Motion field on one frame of our synthetic dance data and (b) motion history from a top view (color indicates frame number).

Since the meshes are consistent over time we were able to obtain the ground truth displacements and to evaluate our results quantitatively. Figure 5 shows the error on the angle of the motion vectors after each regularization step of our algorithm. We can clearly see the advantages of using the normal flow constraints to refine the motion field.

The graphs in Figure 6 show quantitative results on synthetic data. We tested our algorithm on two 15 frame sequences of a sphere seen by 34 cameras.

In the first sequence the motion is a translation and in the second the sphere is rotating on itself. We can see on Figure 6 that the second regularization step (in green) always gives roughly the same level of quality increment. This is due to the fact that our first step (in red) can recover large displacement in such a way that the remaining motion is at sub-pixel level, which is exactly where normal flow information is reliable. Those graphs also show that the quality of our results is not depending on the amplitude of the motion, unlike many other methods.

We also tested our method on a second sequence with only rotational motion, with up to 12 degrees of rotation between two consecutive frames, yielding plots with strictly

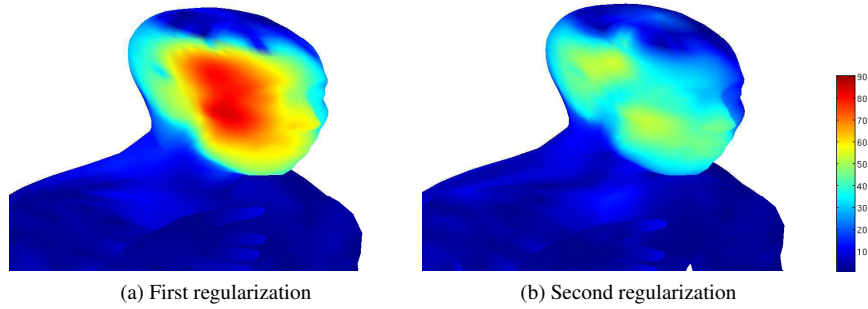


Figure 5: Close-up on the angular error, in degrees, for the dancer's face. This images show how the second step of our method helps recovering motion details.

identical characteristics (not plotted to preserve space). Even if our deformation model does not handle explicitly rotations, as mentioned in section §5.2, we were still able to properly recover the surface motion.

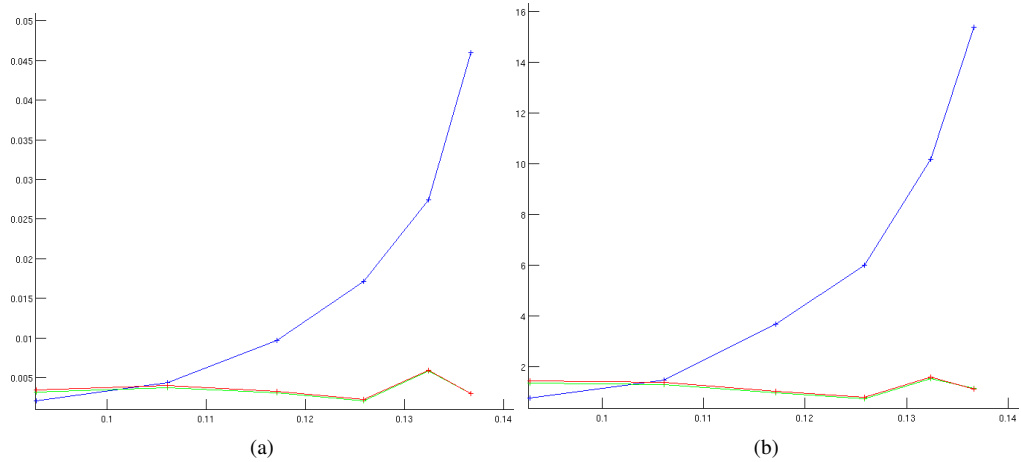


Figure 6: (a) Norm (in meters) and (b) Angular (in degrees) error of the recovered motion with respect to the amount of motion of the surface (in meters). In blue: Vedula *et al.*, in red: our method after the first regularization, and in green: after the second regularization.

6.2 Comparison

In order to compare our approach with the state of the art we implemented Vedula *et al.* method presented in Vedula *et al.* (2005). Since this paper explains three different ways of computing scene flow, we implemented the one which uses the same input information as we do : "Multiple cameras, known scene geometry". We used the latest OpenCV implementation of the Lukas-Kanade optical flow computation with

standard parameters and performed scene flow computation as explained. The graphs in Figure 6 shows the quality of the motion flow computed using Vedula *et al.* (in blue), and compared with our method. As expected our approach clearly outperform the other method as soon as the motion of the object is bigger than pixel size in the images.

Note that the quality of our results is correlated with the resolution of the model used. While Vedula *et al.* are performing regularization in image space, we are performing our regularization on the discretized surface. Thus we could improve our results by using higher resolution models (at a higher tessellation level).

6.3 Experiments on Real Data

We computed 3D motion fields on the popular *flashkick* sequence. In this challenging sequence the subject is wearing loose clothes with poor texture information. Furthermore, the amplitude of the motion is really high between two frames. Fewer reliable 2D/3D correspondences are available, but they are mandatory to recover the wide displacement.

We however succeeded to compute a coherent motion field on most of the frames (see Figures 7-a-b). On a few frames where our algorithm did not find any features on the legs or feet of the dancer, the computed motion field shows the good direction but not the correct norm of the vectors. Lack of visual constraints results in incomplete first estimation of the motion field, the remaining displacement cannot be recovered completely by the normal flow constraints. Figure 7-c) shows a problematic frame where the motion of the right leg of the dancer is not properly computed. To visualize this error, we displayed the input surfaces at time t and $t+1$ (respectively cyan and dark blue), while the *flowed* surface is shown in yellow dots. Finally figure 7-d) shows the motion history over a few frames. Note that we only compute dense motion over the surface and not a deformed mesh. Thus we do not have a consistent connectivity over time and cannot perform any vertex tracking. Therefore the quantitative evaluation of the data is not possible, but visualization of the results are very satisfactory.

We also used our own sequences. One shows a subject performing a simple action, moving both hands from hips to head. The subject is wearing loose and highly textures clothes which allow to compute a high number of reliable 2D and 3D features, see Figure 8-a-b) for examples of motion fields on this sequence. Figure 8-c) shows the motion field accumulated over the whole sequence. Instantaneous motion field results are shown in Figure 1. They were computed on another of our sequences where the subject falls and stand back up. This sequence involves big motions on the arms which were properly recovered as shown in the motion history in Figure 8-d).

We did a naive hybrid Matlab/C++ implementation of our method and computation time are of the order of a few seconds for each frame on an average intel Core 2 duo computer using a set of 32 2 MPixels images and meshes of 10k vertices.

7 Conclusion

We have presented a unified framework which allows to combine various photometric constraints with the aim compute dense motion information over a surface. This framework is based on an iterative method that allows to handle arbitrary large displacements while still recovering small details. Experiments on real datasets demonstrate the robustness of the approach

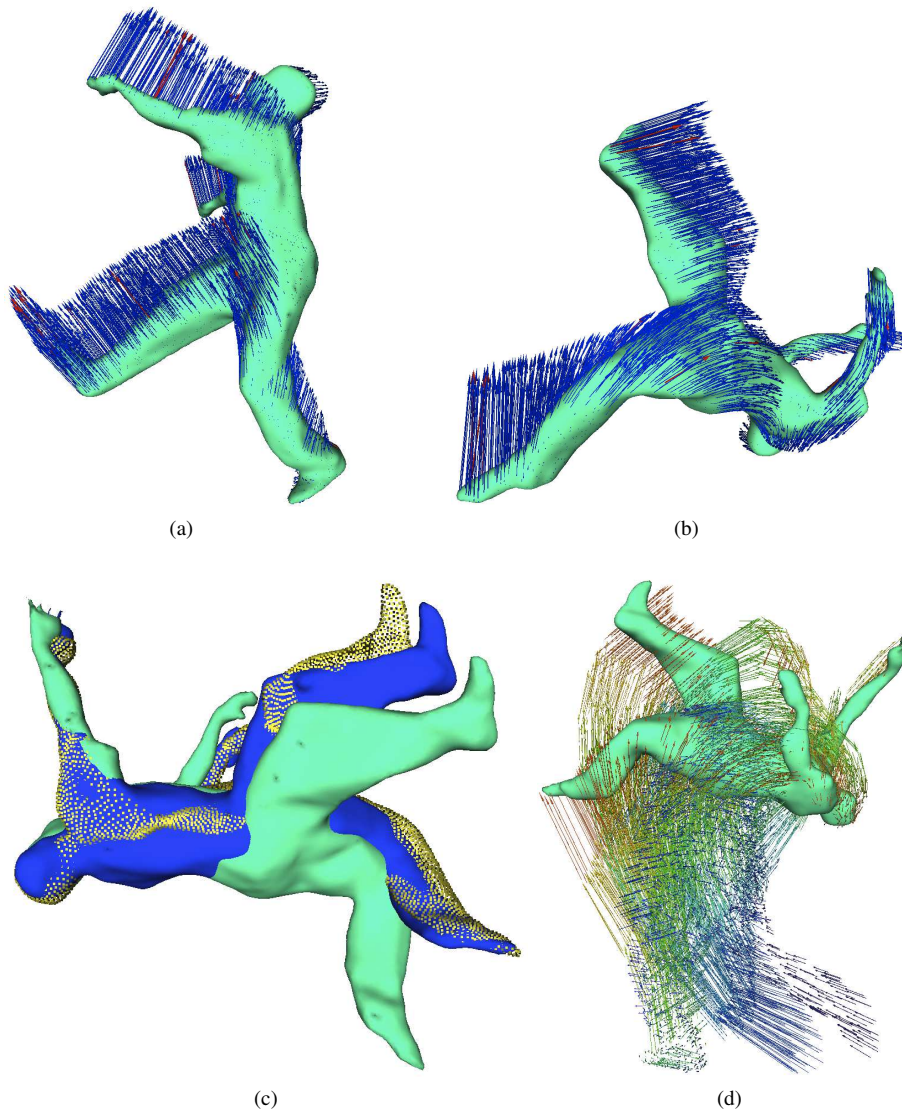


Figure 7: Motion field on challenging frames of the flashkick sequence (a) and (b), partially recovered motion (c) and motion history over this sequence (d) (color indicates frame number).

In order to handle images with less textures, the method could be improved by adding more constraints, for example a photometric consistency criterion such as the one used by Pons *et al.* in Pons *et al.* (2005). Additional perspectives include interactive applications, such as collision-based interactions between the observed object and any virtual object, as well as real-time action recognition.

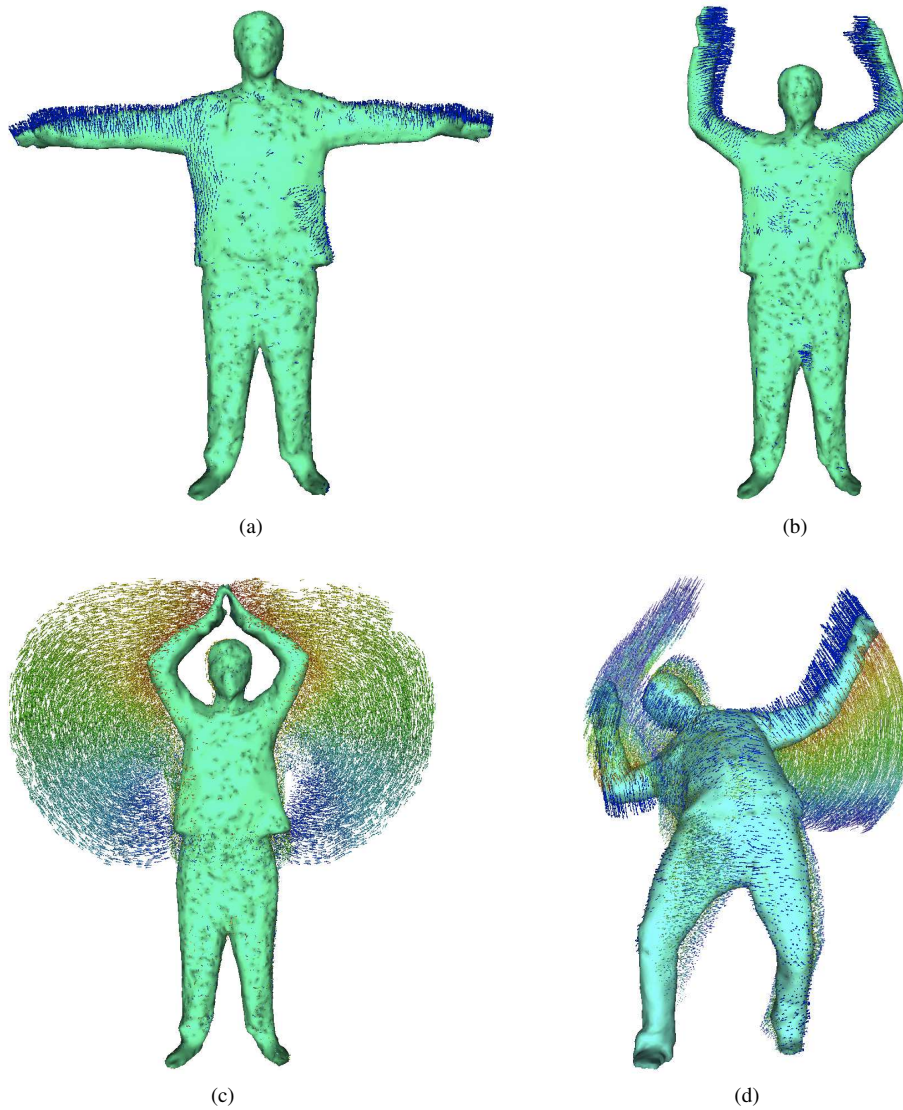


Figure 8: Motion fields on several frames of our real data (a) and (b) and motion history over the sequences (c) and (d) (color indicates frame number).

References

- Barron, J., Fleet, D.-J., and Beauchemin, S. (1994). Performance of Optical Flow Techniques. *International Journal of Computer Vision*.
- Cagniard, C., Boyer, E., and Ilic, S. (2010). Probabilistic Deformable Surface Tracking From Multiple Videos. In *European Conference on Computer Vision*.
- Devernay, F., Mateus, D., and Guilbert, M. (2006). Multi-Camera Scene Flow by Tracking 3-D Points and Surfels. In *Computer Vision and Pattern Recognition*.

- Franco, J.-S. and Boyer, E. (2008). Efficient Polyhedral Modeling from Silhouettes. *IEEE Transactions on Pattern Analysis and Machine Intelligence*.
- Furukawa, Y. and Ponce, J. (2006). Carved Visual Hulls for Image-Based Modeling. In *European Conference on Computer Vision*.
- Horn, B. and Schunck, B. (1981). Determining Optical Flow. *Artificial Intelligence*.
- Isard, M. and MacCormick, J. (2006). Dense Motion and Disparity Estimation via Loopy Belief Propagation. In *Asian Conference on Computer Vision*.
- Liu, C., Yuen, J., Torralba, A., Sivic, J., and Freeman, W. (2008). SIFT Flow: Dense Correspondence across Different Scenes. In *European Conference on Computer Vision*.
- Lowe, D. (2004). Distinctive Image Features from Scale-invariant Keypoints. *International Journal of Computer Vision*.
- Lucas, B. and Kanade, T. (1981). An Iterative Image Registration Technique with an Application to Stereo Vision. In *International Joint Conference on Artificial Intelligence*.
- Naveed, A., Theobalt, C., Rossl, C., Thurn, S., and Seidel, H. (2008). Dense Correspondence Finding for Parametrization-free Animation Reconstruction from Video. In *Computer Vision and Pattern Recognition*.
- Neumann, J. and Aloimonos, Y. (2002). Spatio-Temporal Stereo Using Multi-Resolution Subdivision Surfaces. *International Journal of Computer Vision*.
- Pons, J.-P., Keriven, R., and Faugeras, O. (2005). Modelling Dynamic Scenes by Registering Multi-View Image Sequences. In *Computer Vision and Pattern Recognition*.
- Sorkine, O. and Alexa, M. (2007). As-Rigid-As-Possible Surface Modeling. In *Eurographics Symposium on Geometry Processing*.
- Starck, J. and Hilton, A. (2007a). Correspondence Labeling for Wide-Timeframe Free-Form Surface Matching. In *European Conference on Computer Vision*.
- Starck, J. and Hilton, A. (2007b). Surface Capture for Performance-Based Animation. *IEEE Computer Graphics and Applications*.
- Varanasi, K., Zaharescu, A., Boyer, E., and Horaud, R. P. (2008). Temporal Surface Tracking Using Mesh Evolution. In *European Conference on Computer Vision*.
- Vedula, S., Baker, S., Rander, P., Collins, R., and Kanade, T. (2005). Three-Dimensional Scene Flow. *IEEE Transactions on Pattern Analysis and Machine Intelligence*.
- Wedel, A., Rabe, C., Vaudrey, T., Brox, T., Franke, U., and Cremers, D. (2008). Efficient Dense Scene Flow from Sparse or Dense Stereo Data. In *European Conference on Computer Vision*.
- Xu, L., Jia, J., and Matsushita, Y. (2010). Motion Detail Preserving Optical Flow Estimation. In *Computer Vision and Pattern Recognition*.

- Zaharescu, A., Boyer, E., Varanasi, K., and Horaud, R. P. (2009). Surface Feature Detection and Description with Applications to Mesh Matching. In *Computer Vision and Pattern Recognition*.
- Zhang, Y. and Kambhamettu, C. (2001). On 3D Scene Flow and Structure Estimation. In *Computer Vision and Pattern Recognition*.



Centre de recherche INRIA Grenoble – Rhône-Alpes
655, avenue de l'Europe - 38334 Montbonnot Saint-Ismier (France)

Centre de recherche INRIA Bordeaux – Sud Ouest : Domaine Universitaire - 351, cours de la Libération - 33405 Talence Cedex
Centre de recherche INRIA Lille – Nord Europe : Parc Scientifique de la Haute Borne - 40, avenue Halley - 59650 Villeneuve d'Ascq
Centre de recherche INRIA Nancy – Grand Est : LORIA, Technopôle de Nancy-Brabois - Campus scientifique
615, rue du Jardin Botanique - BP 101 - 54602 Villers-lès-Nancy Cedex
Centre de recherche INRIA Paris – Rocquencourt : Domaine de Voluceau - Rocquencourt - BP 105 - 78153 Le Chesnay Cedex
Centre de recherche INRIA Rennes – Bretagne Atlantique : IRISA, Campus universitaire de Beaulieu - 35042 Rennes Cedex
Centre de recherche INRIA Saclay – Île-de-France : Parc Orsay Université - ZAC des Vignes : 4, rue Jacques Monod - 91893 Orsay Cedex
Centre de recherche INRIA Sophia Antipolis – Méditerranée : 2004, route des Lucioles - BP 93 - 06902 Sophia Antipolis Cedex

Éditeur
INRIA - Domaine de Voluceau - Rocquencourt, BP 105 - 78153 Le Chesnay Cedex (France)
<http://www.inria.fr>
ISSN 0249-6399